GEOPHYSICS. VOL. 76, NO. 6 (NOVEMBER-DECEMBER 2011); P. WC127–WC142, 15 FIGS., 2 TABLES.
10.1190/GEO2010-0408.1

Narrow-angle representations of the phase and group velocities and their applications in anisotropic velocity-model building for microseismic monitoring

Vladimir Grechka[1] and Anton A. Duchkov[2]

ABSTRACT

It is usually believed that angular aperture of seismic data should be at least 20° to allow estimation of the subsurface anisotropy. Although this is certainly true for reflection data, for which anisotropy parameters are inverted from the stacking velocities or the nonhyperbolic moveout, traveltimes of direct P- and S-waves recorded in typical downhole microseismic geometries make it possible to infer seismic anisotropy in angular apertures as narrow as about 10°. To ensure the uniqueness of such an inversion, it has to be performed in a local coordinate frame tailored to a particular data set. Because any narrow fan of vectors is naturally characterized by its average direction, we choose the axes of the local frame to coincide with the polarization vectors of three plane waves corresponding to such a direction. This choice results in a significant simplification of the conventional equations for the phase and group velocities in anisotropic media and makes it possible to predict which elements of the elastic stiffness tensor are constrained by the available data. We illustrate our approach on traveltime synthetics and then apply it to perforation-shot data recorded in a shale-gas field. Our case study indicates that isotropic velocity models are inadequate and accounting for seismic anisotropy is a prerequisite for building a physically sound model that explains the recorded traveltimes.

INTRODUCTION

Much of the progress in the estimation of seismic anisotropy and the building of anisotropic velocity models can be attributed to the choice of appropriate parametrization of the stiffness tensor. Such a parametrization is usually designed to capture the influence of elastic anisotropy on a seismic signature in question and to facilitate the inversion of anisotropy-related quantities from that signature. The most well-known example of reparameterizing the stiffnesses is Thomsen (1986) notation that identifies the combinations of stiffness coefficients of vertically transversely isotropic (VTI) media obtainable in a unique fashion from seismic velocities routinely measured in the exploration practice.

Thomsen parameters are no longer convenient when data contain both kinematic and polarization signatures. The data of this kind, for instance, components of the slowness vectors and directions of the particle motions, are recorded in vertical seismic profiling (VSP) surveys (Zheng and Pšenčík, 2002; Xiao and Leaney, 2010). To estimate seismic anisotropy in the vicinity of downhole geophones from such measurements, one has to define a different set of Thomsen-style parameters, specifically, the one that governs the dependence of the slowness component along a borehole on the direction of the polarization vector and can be unambiguously inverted from this dependence (Grechka and Mateeva, 2007).

Here we examine the same anisotropic parameter-estimation problem but for geometries encountered in downhole microseismic monitoring. The main objective of acquiring microseismic surveys in tight-gas and shale-gas fields is to delineate hydraulic fractures, which are artificially created to make production from low-permeability formations economically viable (e.g., Maxwell, 2010; Maxwell et al., 2010). The shapes and orientations of hydraulic fractures are inferred from locations of microseismic events triggered in the course of hydraulic well stimulations. Clearly, a velocity model is required to locate the microseismicity. This model is conventionally derived from sonic logs and traveltimes of the direct P- and S-waves excited by perforation shots and recorded by geophones placed in an adjacent borehole (e.g., Warpinski et al., 2005; Pei et al., 2009). Hence, the goal of our study is to invert the observed perforation-shot times for a velocity model.

Manuscript received by the Editor 13 December 2010; revised manuscript received 13 June 2011; published online 10 January 2012; corrected version published online 24 January 2012.
[1]Shell Exploration & Production Company, Houston, Texas, USA. E-mail: vladimir.grechka@shell.com.
[2]Institute of Petroleum Geology and Geophysics SB RAS, Novosibirsk, Russia. E-mail: duchkovaa@ipgg.nsc.ru

Although one might think that Thomsen-type parameterization could be helpful in estimating seismic anisotropy from such traveltime data, this is seldom the case. Two typical reasons are narrow angular apertures of ray trajectories recorded by geophones placed in a single well and oblique orientations of those trajectories with respect to layering or principal stress directions, which might be taken as plausible symmetry elements for the elastic properties of the formation. As a consequence of the narrow ray coverage, an analog of the stacking velocity is difficult to measure and, therefore, the δ-type parameters governing the P-wave normal-moveout velocities are poorly constrained. Also, the symmetry-direction velocities used in all Thomsen-style notations lose their significance because the rays from perforation shots generally do not propagate in the vicinity of the symmetry directions.

To resolve these issues and infer anisotropy from perforation-shot data, we propose a strategy that consists of (1) finding a limited subset of the stiffness coefficients that govern the velocities of waves recorded in a given narrow fan of directions and (2) estimating only those particular stiffnesses while leaving the other, not as tightly constrained stiffness components, undetermined. We begin the paper by discussing a coordinate transform that identifies the stiffness coefficients that should be targeted in the inversion, confirm our analytical findings on ray-tracing synthetics, and apply the developed methodology to perforation-shot data from a shale-gas field in the continental United States.

THEORY

Statement of the problem

Consider three plane body waves that have the same unit wavefront normal $\mathbf{n}$ (such waves are termed isonormal) and propagate in a homogeneous anisotropic medium specified by the density-normalized stiffness tensor $\mathbf{c}$. The phase velocities V_Q ($Q = 1, 2, 3$) and the polarization vectors $\mathbf{U}_Q$ of these waves can be found from the Christoffel equation (e.g., Auld, 1973; Červený, 2001)

$$(c_{ijkl} n_j n_k - V_Q^2 \delta_{il}) U_{lQ} = 0, \qquad (i = 1, 2, 3), \qquad (1)$$

where δ_{il} is the 3×3 identity matrix (the so-called Kronecker delta), the subscript $Q = 1, 2, 3$ or $Q = \mathrm{P}, \mathrm{S}_1, \mathrm{S}_2$ is used to denote the wave type (P-, fast shear, or slow shear), and the waves are sorted in accordance with inequalities $V_1 \geq V_2 \geq V_3$ for the phase velocities. Hereinafter, we assume summation from 1 to 3 with respect to all repeating lowercase roman indexes and no summation with respect to uppercase ones.

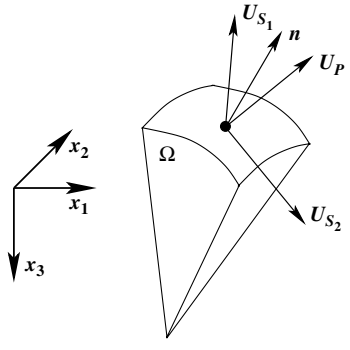

Figure 1. Fan Ω of wave-propagation directions in anisotropic medium.

The group-velocity vectors $\mathbf{g}_Q$ of plane waves are given by (e.g., Auld, 1973; Červený, 2001)

$$g_{jQ} = c_{ijkl} U_{iQ} \mathbf{p}_{kQ} U_{lQ}, \qquad (j, Q = 1, 2, 3), \qquad (2)$$

where

$$\mathbf{p}_Q = \mathbf{n}/V_Q \qquad (3)$$

are the slowness vectors. The (scalar) group velocities are defined as

$$g_Q = |\mathbf{g}_Q| \equiv \sqrt{\mathbf{g}_Q \cdot \mathbf{g}_Q}. \qquad (4)$$

Suppose we compute $g_Q(\mathbf{n})$ from equations 1–4 for a set of the wavefront normals $\mathbf{n} \in \Omega$ (Figure 1). We would like to know which components of tensor $\mathbf{c}$ are constrained by velocities V_Q or g_Q, especially when the directions of vectors $\mathbf{n}$ compose a narrow fan Ω.

Examples

A solution to the problem posed above appears to depend on the orientation of fan Ω with respect to the symmetry elements of a given anisotropic solid. Let us illustrate this statement with two simple examples, for which we take an orthorhombic medium that has Tsvankin's (1997) coefficients $V_{\mathrm{P0}} = 3$ km/s, $V_{\mathrm{S0}} = 1.3$ km/s, $\epsilon^{(1)} = 0.4$, $\epsilon^{(2)} = 0.2$, $\delta^{(1)} = 0.1$, $\delta^{(2)} = 0.3$, $\delta^{(3)} = -0.2$, $\gamma^{(1)} = 0.15$, and $\gamma^{(2)} = -0.2$ or the density-normalized stiffness matrix (in km^2/s^2)

$$\mathbf{c} = \begin{pmatrix} 12.600 & 5.272 & 7.949 & 0 & 0 & 0 \\ 5.272 & 16.200 & 2.511 & 0 & 0 & 0 \\ 7.949 & 2.511 & 9.000 & 0 & 0 & 0 \\ 0 & 0 & 0 & 3.662 & 0 & 0 \\ 0 & 0 & 0 & 0 & 1.690 & 0 \\ 0 & 0 & 0 & 0 & 0 & 2.197 \end{pmatrix}. \qquad (5)$$

Matrix 5 represents stiffness tensor $\mathbf{c}$ in Voigt notation, which is defined by substitutions $11 \to 1$, $22 \to 2$, $33 \to 3$, $23 \to 4$, $13 \to 5$, and $12 \to 6$ for the pairs of indexes (ij) and (kl) of tensor c_{ijkl}.

In our first example, we choose a set of the wavefront normals

$$\mathbf{n} = [\sin\theta_1 \cos\theta_2, \sin\theta_1 \sin\theta_2, \cos\theta_1] \qquad (6)$$

whose polar angles θ_1 and azimuths θ_2 belong to the fan

$$\Omega = [89^\circ \leq \theta_1 \leq 91^\circ, -1^\circ \leq \theta_2 \leq +1^\circ]. \qquad (7)$$

Because the directions of $\mathbf{n}$ within Ω concentrate in a close vicinity of the axis $\mathbf{x}_1$, either velocities V_Q or g_Q constrain three elements c_{11}, c_{55}, and c_{66} of the stiffness matrix 5. This follows from equations 1–4, which result in equalities $V_1 = g_1 = \sqrt{c_{11}}$, $V_2 = g_2 = \sqrt{c_{66}}$, and $V_3 = g_3 = \sqrt{c_{55}}$ for $\mathbf{n} = [1, 0, 0]$. If velocities of one wave mode (for instance, slow S-wave) are unavailable, the corresponding stiffness coefficient (c_{55}, in this particular example) cannot be determined. Whether or not it is possible to estimate

other stiffness components from the velocities measured for directions **n** in fan 7 requires further investigation; this issue is addressed below.

In our second example, we change fan 7 to

$$\Omega = [44^\circ \le \theta_1 \le 46^\circ, 44^\circ \le \theta_2 \le 46^\circ]. \quad (8)$$

If we now substitute the wavefront normals **n** (equation 6) whose directions are given by angles 8 into the Christoffel equation 1, all nonzero stiffness elements in matrix 5 also appear in the Christoffel matrix $\Gamma_{il} \equiv c_{ijkl} n_j n_k$ $(i, l = 1, 2, 3)$. Such a result suggests that the phase velocities might depend on all nine orthorhombic c_{IJ}s, rather than on their small subset, which was the case in the previous example. Switching from the stiffnesses to Tsvankin's (1997) notation leads to a similar conclusion. Indeed, the weak anisotropy approximation of the P-wave phase velocity V_P given by equations 1.107–1.109 in Tsvankin (2001) contains five anisotropy coefficients: $\epsilon^{(1)}$, $\epsilon^{(2)}$, $\delta^{(1)}$, $\delta^{(2)}$, and $\delta^{(3)}$ multiplied by comparable trigonometric factors, which range from 1/16 to 3/16 for $\theta_1 = \theta_2 = 45^\circ$. Hence, all five anisotropy coefficients influence V_P in a significant manner. Their estimation from the P-wave velocities in the examined fan Ω (equation 8), however, is likely to be ambiguous.

Singular value decomposition

The qualitative assessment of the uniqueness of the inversion made in the previous section can be quantified by computing the Frechét derivatives $\boldsymbol{\mathcal{F}}_V \equiv [\partial V_Q / \partial c_{IJ}]$ and $\boldsymbol{\mathcal{F}}_g \equiv [\partial g_Q / \partial c_{IJ}]$ of the velocities with respect to the stiffness components. Matrices, in which derivatives with respect to each c_{IJ} form the column-vectors, are derived in Appendix A. Applying the SVD to either matrix $\boldsymbol{\mathcal{F}}_V$ or $\boldsymbol{\mathcal{F}}_g$, we represent it as the product of three matrices: a column-orthogonal matrix **u**, a diagonal matrix **s**, whose positive or zero elements known as the singular values are conventionally arranged in the descending order, and the transpose of an orthogonal eigenvector matrix **w** (e.g., Press et al., 2003):

$$\boldsymbol{\mathcal{F}}_A = \mathbf{u}_A \mathbf{s}_A \mathbf{w}_A^T, \quad (9)$$

where the subscript $A = V$ or $A = g$ denotes the phase or group velocity, respectively.

To illustrate the usefulness of this approach, we apply it to the second example from the previous section. Figure 2 shows the singular values and eigenvectors of matrices $\boldsymbol{\mathcal{F}}_V$ and $\boldsymbol{\mathcal{F}}_g$ computed for the P-, S_1-, and S_2-waves propagating along the wavefront normal directions that belong to fan 8. An intuitive understanding that our narrow-angle data constrain just the P-, S_1-, and S_2-wave velocities in the vicinity of $\theta_1 = \theta_2 = 45^\circ$ is corroborated by the presence of a pronounced drop in the singular values after the three greatest ones, which presumably correspond to those velocities. A difference between the third and the fourth singular values (approximately by a factor of 30) suggests that perhaps only three stiffness combinations can be recovered from noise-contaminated velocities. The eigenvector matrices (gray squares), however, indicate that all nine orthorhombic stiffness coefficients contribute to these combinations, leading to an obvious ambiguity in the inversion for c_{IJ}s: three equations cannot be uniquely solved for nine unknowns.

As expected, Figures 2a and 2b look very similar because the Frechét-derivative matrices $\boldsymbol{\mathcal{F}}_V$ and $\boldsymbol{\mathcal{F}}_g$ coincide in weakly anisotropic media. Their identity for weak anisotropy follows from the well-known equality $V_Q(\mathbf{n}) = g_Q(\mathbf{r})$, in which the group velocity is evaluated along the ray direction $\mathbf{r} \equiv \mathbf{g}_Q / g_Q$. Although the equality $\boldsymbol{\mathcal{F}}_V = \boldsymbol{\mathcal{F}}_g$ is satisfied only approximately in moderately and strongly anisotropic media, it allows us to restrict our further analysis to either matrix $\boldsymbol{\mathcal{F}}_V$ or $\boldsymbol{\mathcal{F}}_g$. In practice, the choice of inverting either phase or group velocities would depend on a particular data processing goal. For example, a local slowness (reciprocal to the phase velocity) component along a borehole can be always computed from arrival times measured on a common-shot gather (e.g., Zheng and Pšenčík, 2002; Grechka and Mateeva, 2007). On the other hand, the group velocities, needed to model the traveltimes, are useful for estimating the effective medium properties, such as those discussed in our field-data example below.

Performing the SVD for the phase velocities in the wavefront normal fan 7 results in the singular values and eigenvectors displayed in Figure 3. This time, eigenvector matrix $\mathbf{w}_V$ is quite sparse and the elements of $\mathbf{w}_V$ corresponding to c_{11}, c_{55}, and c_{66} are the only significant entries in the first three columns that contain the combinations of stiffness coefficients constrained by the three greatest singular values. Thus, these coefficients can be unambiguously estimated from the measured velocities. Although we foresaw such an outcome in the previous section, the SVD provides additional information. The high ratio of the third and the fourth singular values $s_{V,33}/s_{V,44} \sim 10^3$ in Figure 3 suggests that nothing except for c_{11}, c_{55}, and c_{66} can be estimated from the velocities contaminated with any realistic noise.

Comparison of the SVDs in Figures 2 and 3 might lead one to conclude that the ability to infer stiffnesses in anisotropic media from the velocity measurements primarily depends on the direction of wave propagation. In the next section, we show that this is not the

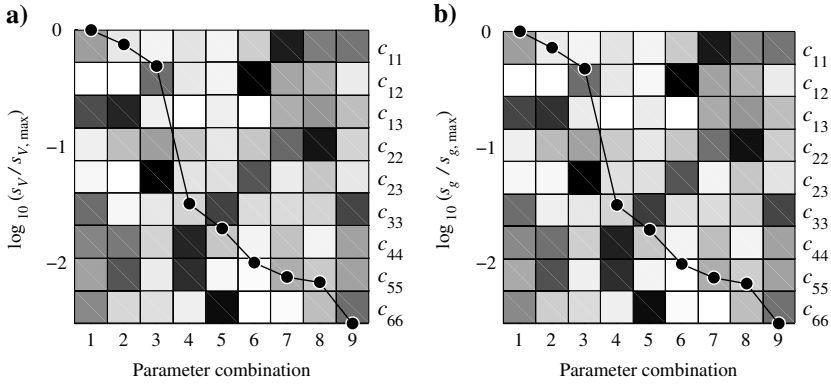

Figure 2. Logarithms of normalized singular values (black dots) plotted on top of the absolute values of elements of the eigenvector matrices **w** (gray squares) for phase (a) and group (b) velocities. The rows of **w** are arranged in the order of stiffness components shown on the right. Each column of **w** is an eigenvector that corresponds to the singular value (black dot) shown in that column. The black color of the squares denotes $|w_{ij}| = 1$, whereas white $- w_{ij} = 0$; the color scale is linear. Computations are performed for the stiffness matrix 5 and fan Ω of 25 wavefront normal directions defined by inequalities 8. The directions are spaced at increments of 0.5° in both θ_1 and θ_2.

case and certain stiffness coefficients can be always obtained in a unique and robust fashion in a specially rotated coordinate system.

Solution

Here we discuss a coordinate transform designed to make many elements of matrix $\mathbf{w}_V$ close to zero for an arbitrary orientation of narrow fan Ω of the wave-propagation directions. We choose the matrix $\mathbf{U}^T$ of our transform to be the transpose of the orthogonal polarization vectors $\mathbf{U}_Q$ of three isonormal waves propagating along an arbitrarily selected wavefront normal $\mathbf{n}$ within Ω. Applying the Bond transformation (e.g., Auld, 1973) with matrix $\mathbf{U}^T$ to stiffness tensor $\mathbf{c}$ produces tensor $\mathbf{c}'$ that generally has no zero elements (Helbig, 1994) and appears as the one describing a triclinic solid even when the original anisotropic medium has a higher symmetry. Importantly, the polarization vectors $\mathbf{U}'$ after the transform,

$$\mathbf{U}' = \mathbf{U}^T\mathbf{U} = U_{il}U_{jl} = \delta_{ij}, \qquad (i,j = 1,2,3) \tag{10}$$

are oriented along the new coordinate axes $\mathbf{x}_i'$, as is schematically shown in Figure 4.

Phase velocity

The simplification expressed by equation 10 is critical for gaining an analytic insight into which stiffness coefficients control the phase and group velocities of plane waves propagating in direction

$$\mathbf{n}' = \mathbf{U}^T\mathbf{n}. \tag{11}$$

Indeed, according to the Christoffel equation 1, the squared phase velocities are

$$V_Q^2 = c'_{QjkQ}n'_jn'_k, \qquad (Q = 1,2,3), \tag{12}$$

or, in expanded form,

$$V_P^2 \equiv V_1^2 = \underbrace{c'_{11}(n'_1)^2}_{\text{(i)}} + \underbrace{[2c'_{16}n'_1n'_2 + 2c'_{15}n'_1n'_3]}_{\text{(ii)}} + \underbrace{[c'_{66}(n'_2)^2 + 2c'_{56}n'_2n'_3 + c'_{55}(n'_3)^2]}_{\text{(iii)}}, \tag{13}$$

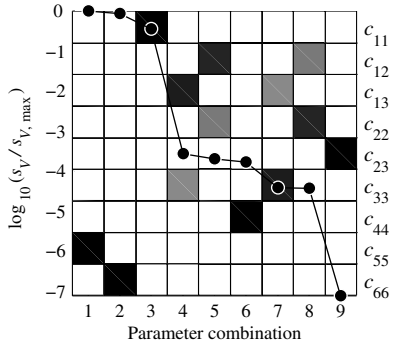

Figure 3. The same as Figure 2a but for the wavefront normal fan Ω given by inequalities 7.

$$V_{S_1}^2 \equiv V_2^2 = \underbrace{c'_{66}(n'_1)^2}_{\text{(i)}} + \underbrace{[2c'_{26}n'_1n'_2 + 2c'_{46}n'_1n'_3]}_{\text{(ii)}} + \underbrace{[c'_{22}(n'_2)^2 + 2c'_{24}n'_2n'_3 + c'_{44}(n'_3)^2]}_{\text{(iii)}}, \tag{14}$$

$$V_{S_2}^2 \equiv V_3^2 = \underbrace{c'_{55}(n'_1)^2}_{\text{(i)}} + \underbrace{[2c'_{45}n'_1n'_2 + 2c'_{35}n'_1n'_3]}_{\text{(ii)}} + \underbrace{[c'_{44}(n'_2)^2 + 2c'_{34}n'_2n'_3 + c'_{33}(n'_3)^2]}_{\text{(iii)}}. \tag{15}$$

Equations 13–15 are exact for plane waves. To reveal their significance, we notice that in most anisotropic materials the P-wave polarization vector deviates from the wavefront normal by a few degrees; that is, $\mathbf{n} \approx \mathbf{U}_P$ (e.g., Tsvankin, 2001). Hence, $\mathbf{n}' \approx \mathbf{x}_1' = [1,0,0]'$ and the terms in equations 13–15 can be placed into groups (i), (ii), and (iii) in accordance with their magnitudes expressed by inequalities

$$|n'_1|^2 \gg |n'_1n'_j| \gg |n'_jn'_k|, \qquad (j,k = 2,3). \tag{16}$$

Although the inequalities 16 might break down for extremely strong anisotropy (Helbig and Schoenberg, 1987), they are expected to be valid for typical anisotropic rocks encountered in the subsurface.

Combining equations 13–15 with inequalities 16, we conclude that stiffness coefficients c'_{11}, c'_{66}, and c'_{55} are best constrained by the P-, S_1-, and S_2-wave velocities in narrow-angle geometries. These coefficients comprise group (i) in equations 13–15. This

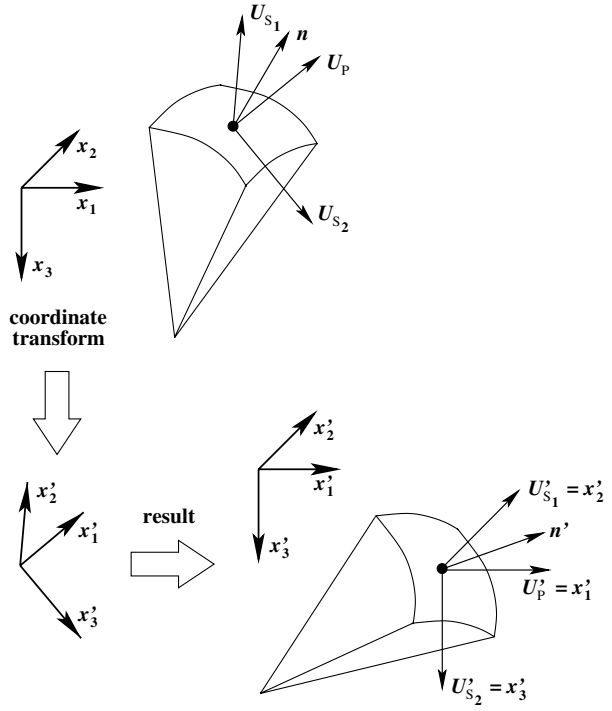

Figure 4. Coordinate rotation that aligns the new axes $\mathbf{x}_i'$ with the polarization vectors.

finding is hardly surprising in light of our discussion in the previous sections. Stiffnesses c'_{11}, c'_{66}, and c'_{55} are followed by six c'_{IJ}s grouped in (ii) in 13–15. All stiffnesses in groups (iii) in equations 13–15, except for c'_{55} and c'_{66} that already appear in (i), are not as tightly constrained. The fourth group consists of six coefficients c'_{12}, c'_{13}, c'_{14}, c'_{23}, c'_{25}, and c'_{36}, which are not present in equations 13–15. For this reason, their estimation in the examined geometries should be regarded as questionable.

The last statement might be better understood if we notice that c'_{12}, c'_{13}, and c'_{23} are related to Tsvankin's δ-coefficients that control the P-wave normal-moveout (NMO) velocities in orthorhombic media (Tsvankin, 1997; Grechka and Tsvankin, 1999). Because the NMO velocities cannot be accurately estimated in our narrow fans of wave-propagation directions, one might expect large errors in the δ-coefficients and, consequently, in the stiffnesses c'_{12}, c'_{13}, and c'_{23}.

A qualitative discussion above is, in fact, directly supported by the SVD. Figure 5 shows the singular values and the eigenvector matrix for the orthorhombic model given by equation 5 but performed with respect to the Bond-transformed stiffness coefficients $\mathbf{c}'$ with matrix

$$\mathbf{U}^T = \begin{pmatrix} 0.529 & 0.565 & 0.634 \\ 0.350 & -0.825 & 0.444 \\ 0.774 & -0.013 & -0.634 \end{pmatrix}, \qquad (17)$$

which is obtained from the polarization vectors of waves that have the wavefront normal $\mathbf{n} = [1, 1, \sqrt{2}]/2$. The rows of matrix $\mathbf{w}_V$ in Figure 5 are sorted to make the eigenvector matrix as diagonally dominant as possible. Such a sorting is helpful because a diagonal eigenvector matrix would be ideal for the inversion. Although matrix $\mathbf{w}_V$ in Figure 5 is not diagonal, it has a large number of zero and nearly zero elements (compare with Figure 2), which imply that information about each stiffness coefficient c'_{IJ} is concentrated in the respective singular value and relatively little trade-off between different c'_{IJ}s is expected. The lower the position of a given c'_{IJ} on the right-hand side of Figure 5, the less tightly it is constrained by the data.

Let us note a staircase behavior of the singular values (dots in Figure 5) predicted by equations 13–15. Indeed, the three greatest singular values correspond to c'_{55}, c'_{66}, and c'_{11} in accordance with equations 13–15. The next six parameter combinations in Figure 5 are dominated by the stiffnesses c'_{15}, c'_{16}, c'_{45}, c'_{46}, c'_{35}, and c'_{26} that appear in groups (ii) in equations 13–15. Their order depends on the relative magnitudes of the wavefront normal components n'_2 and n'_3 and, thus, unimportant for our discussion. Although the exact number of c'_{IJ}s that can be estimated from the velocities depends on the noise level, the remaining 12 stiffnesses are unlikely to be accurately recovered because the normalized singular values corresponding to them are smaller than 10^{-3}.

Because one's ability of inferring certain stiffness components significantly depends on the data aperture, it is important to investigate whether our previous assessment holds when solid angles of the wavefront normal directions cover more than just a few square degrees. To address this issue, we open up the data aperture by a factor of approximately 100 (by increasing the ranges of both angles θ_1 and θ_2 10 times) and repeat the previous numerical experiment. The result in Figure 6 indicates that equations 13–15 keep predicting the correct order of sensitivities of the phase velocities to c'_{IJ}s, even though the staircase behavior of the singular values (black dots) disappears and their overall range gets smaller. Both those features are expected because of the widening of the data aperture.

Group velocity

The use of polarization vectors expressed by equation 10 is especially beneficial for the group velocities. Transforming equation 2 to the rotated coordinate frame yields

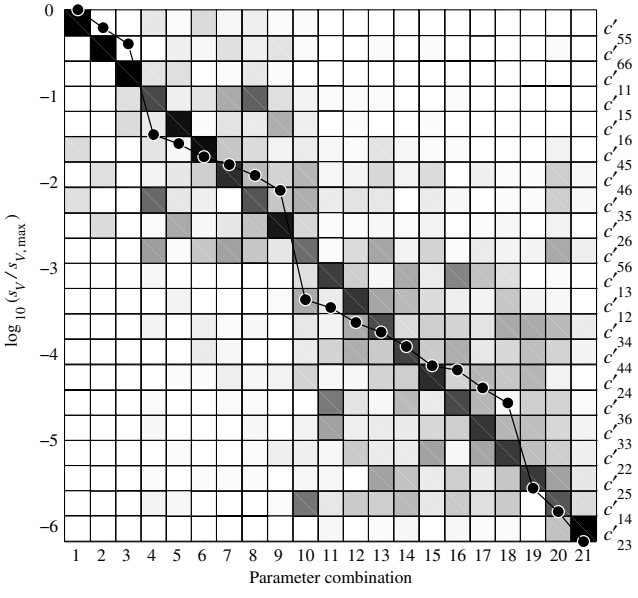

Figure 5. Logarithms of normalized singular values (black dots) and absolute values of the elements of eigenvector matrix $\mathbf{w}_V$ (gray squares) in a coordinate frame rotated with matrix 17. The rows of $\mathbf{w}_V$ are sorted to make it as diagonally dominant as possible. The fan Ω of the wavefront normal directions is given by inequalities 8.

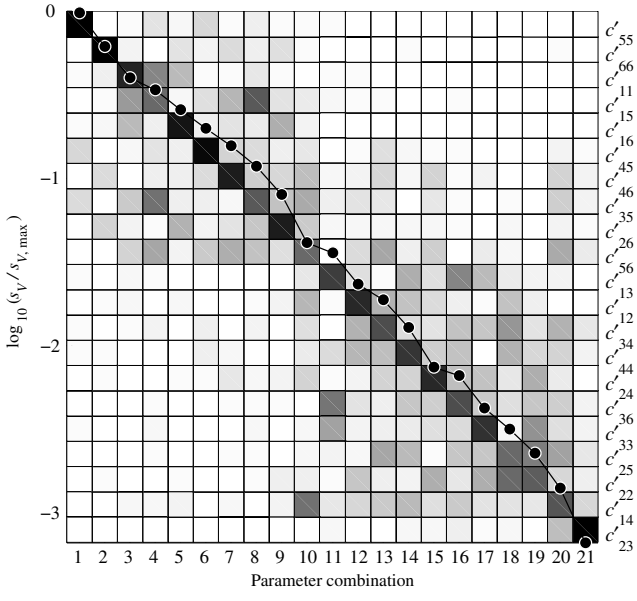

Figure 6. The same as Figure 5 but for a fan of polar angles θ_1 and azimuths θ_2 of the wavefront normals $\Omega = [35^\circ \le \theta_1 \le 55^\circ, 35^\circ \le \theta_2 \le 55^\circ]$.

$$g'_{jQ} = c'_{QjkQ} p'_{kQ}, \quad (j, Q = 1, 2, 3), \tag{18}$$

where $\mathbf{p}'_Q = \mathbf{n}'_Q / V_Q$ are the rotated slowness vectors. Introducing the 3×3 symmetric positive-definite matrices

$$\boldsymbol{\mathcal{V}}'_Q \equiv \mathcal{V}'_{jkQ} = c'_{QjkQ} \qquad (j, k, Q = 1, 2, 3), \tag{19}$$

which are related to the so-called Voigt stiffness tensor $\mathbb{V}'$ (Cowin, 1989; Helbig, 1994) as $\mathbb{V}' = \sum_{Q=1}^{3} \boldsymbol{\mathcal{V}}'_Q$, we rewrite equation 18 in the form of a product of matrix $\boldsymbol{\mathcal{V}}'_Q$ and vector $\mathbf{p}'_Q$

$$\mathbf{g}'_Q = \boldsymbol{\mathcal{V}}'_Q \mathbf{p}'_Q, \qquad (Q = 1, 2, 3). \tag{20}$$

One can easily verify that the inverse relationship $\mathbf{p}'_Q = (\boldsymbol{\mathcal{V}}'_Q)^{-1} \mathbf{g}'_Q$ is also valid.

To the best of our knowledge, equation 20 is the simplest exact equation for the group velocities of plane waves propagating in triclinic media. It turns out to be the most computationally efficient too. Table 1 compares the cost of applying equation 20 with those of other known equations. While the group velocities calculated with various equations are numerically identical, the computational expenses differ substantially. We see that equation 20 performs particularly well when $\mathbf{g}_Q$ of all three isonormal waves have to be computed. This happens because transformation $\mathbf{c} \to \mathbf{c}'$ needs to be applied only once. Even for a single wave mode, however, equation 20 is superior to all its competitors. Although the issue of the efficient calculation of the group velocities might seem insignificant, we note that this computation comprises the innermost core of any anisotropic ray-tracing code and, therefore, directly influences the overall performance of all subsequent traveltime calculations.

Like equation 12, which can be written in terms of matrices $\boldsymbol{\mathcal{V}}'_Q$ as

$$V_Q^2 = \mathbf{n}'^T \boldsymbol{\mathcal{V}}'_Q \mathbf{n}', \qquad (Q = 1, 2, 3), \tag{21}$$

equation 20 leads to representation

$$g_Q^2 = \mathbf{p}'^T_Q (\boldsymbol{\mathcal{V}}'_Q)^2 \mathbf{p}'_Q, \qquad (Q = 1, 2, 3) \tag{22}$$

and results in analytic expressions of the group velocities similar to those given by equations 13–15. We do not present these expressions here because they are rather lengthy and entail the same conclusions pertaining to the sensitivities of g_Q to c'_{IJ}s as those that we have already discussed for the sensitivities of V_Q.

Figure 7 exemplifies this statement. We performed the SVD for the same fan of the wavefront normal directions as that in Figure 5 but used only two group velocities, g_P and g_{S_1}, to construct the Frechét-derivative matrix $\boldsymbol{\mathcal{F}}_g$. The absence of the slow shear-wave data is evident in Figure 7. The stiffness coefficients contributing to the singular values greater than 10^{-3} are exactly those that appear in groups (i) and (ii) in equations 13 and 14. They are separated from the rest of the stiffnesses in Figure 7 by a large drop in the singular values (black dots), which likely divides the c'_{IJ}s into those that can and cannot be realistically recovered from the velocities.

Table 1. Relative computing time spent on calculation of the group velocities with various equations. The codes are written in MATLAB; the computations are performed on a single processor. The last two columns in the table correspond to direct differentiation of the phase velocity V with respect to the wavefront normal $\mathbf{n}$ and to computations using equations B3 and B4 in Grechka et al. (1999), which express $\mathbf{g}$ in terms of the slowness vector $\mathbf{p}$ and its derivatives.

The number of isonormal waves	Equation 20	Equation 2	$\mathbf{g} = \partial V / \partial \mathbf{n}$	$\mathbf{g} = \mathbf{f}(\mathbf{p})$
1	1	1.6	2.8	3.0
2	1	1.9	4.0	5.3
3	1	2.1	5.0	7.5

INVERSION OF PHASE VELOCITIES

Having shown that inversion of the phase, V_Q, and group, g_Q, velocities with respect to the stiffness coefficients needs to be performed in a local coordinate frame, which relates to a given narrow-angle data geometry, we proceed with estimation of these stiffnesses. Because V_Q and g_Q depend on the stiffness components in a similar manner (compare Figure 2a and 2b), we discuss inversion of the phase velocities in this section and turn our attention to the group velocities in the next section, where we examine our field data.

Here we compute the phase velocities in a narrow fan of the wavefront normal directions (described in the caption to Figure 8), add a 0.5% Gaussian noise to the velocity values and invert these noise-contaminated velocities for the stiffness coefficients. An important consequence of the fact that our velocities are inherently incapable of constraining all elements of stiffness tensor $\mathbf{c}'$ is that we have to devise a strategy for infilling the c'_{IJ}s that cannot be inferred from the available data. While several choices for such an infill strategy exist (see the Discussion section), we opt for perhaps the simplest one, which is to make $\mathbf{c}'$ as close to isotropy as possible at each stage of the inversion. Appendix B describes the operational details of our approach.

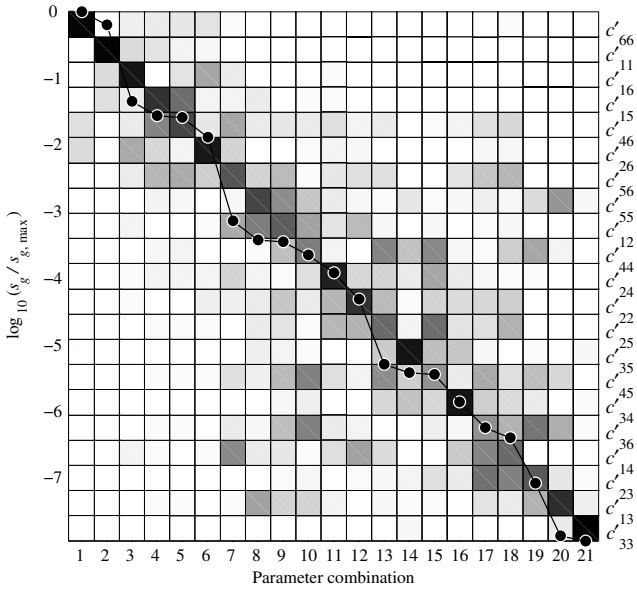

Figure 7. The same as Figure 5 but for the group, rather than phase velocities, and when only the P- and fast S-waves are available.

Our inversion procedure is organized as follows. We begin with the SVD of the Frechét-derivative matrix constructed for a purely isotropic model. The velocities in this model are unimportant because the goal of this SVD is just to reveal a sequence of c'_{IJ}s that we then iteratively target in the least-squares, nonlinear, gradient-based inversion. In this section, we use the same orthorhombic model as before (equation 5) so that the column of stiffness elements on the right-hand side of Figure 8a represents the order in which the c'_{IJ}s are estimated in our first test. Next, we select the number of stiffnesses to be obtained at the initial nonlinear iteration of the inversion. Because the noise-contaminated velocities of all three wave modes are used and the S-waves exhibit splitting, it makes sense to honor it and invert the velocities for three best constrained stiffness coefficients c'_{66}, c'_{55}, and c'_{11}. The inversion results in 1.4% root-mean-square (RMS) error in the velocities (the leftmost dot in Figure 8b).

We use the estimated c'_{66}, c'_{55}, c'_{11} as an initial guess for the second iteration of the nonlinear inversion, in which we add another unknown c'_{15} (see the right-hand side column in Figure 8a) and update all four stiffnesses. This inversion step yields a slightly smaller RMS error (Figure 8b). We keep adding one stiffness coefficient at a time, updating all relevant c'_{IJ}s, and observing the reduction in the RMS error. At some point, specifically, after adding the ninth stiffness coefficient, the RMS error reaches the level comparable to that of noise (0.5%) and does not significantly decrease any further (Figure 8b). Our interpretation of such a behavior is that the top nine c'_{IJ}s in Figure 8a are sufficient to explain the data; when we relax other stiffnesses, we start fitting the noise. Therefore, it is important to find out whether the nine stiffness coefficients result in a satisfactory solution in the model space.

To do so, we calculate the Bond transformation of the exact tensor $\mathbf{c}$ (equation 5) with matrix $\mathbf{U}^T$ (equation 17)

$$\mathbf{c}' = \begin{pmatrix} 10.869 & 5.216 & 6.596 & 1.136 & 0.492 & -0.658 \\ 5.216 & 12.837 & 5.264 & 0.182 & 1.378 & -1.909 \\ 6.596 & 5.264 & 11.409 & 0.451 & 0.698 & 1.634 \\ 1.136 & 0.182 & 0.451 & 2.353 & -0.630 & -0.374 \\ 0.492 & 1.378 & 0.698 & -0.630 & 1.869 & 0.028 \\ -0.658 & -1.909 & 1.634 & -0.374 & 0.028 & 4.664 \end{pmatrix}. \tag{23}$$

This tensor is to be compared with the inverted stiffness tensor (in $\mathrm{km}^2/\mathrm{s}^2$)

$$\mathbf{c}'^{(\mathrm{inv})} = \begin{pmatrix} \mathbf{10.885} & 4.335 & 4.335 & 0 & \mathbf{0.427} & \mathbf{-0.695} \\ 4.335 & 10.885 & 4.335 & 0 & 0 & \mathbf{-1.847} \\ 4.335 & 4.335 & 10.885 & 0 & \mathbf{0.648} & 0 \\ 0 & 0 & 0 & 3.275 & \mathbf{-0.761} & \mathbf{-0.240} \\ \mathbf{0.427} & 0 & \mathbf{0.648} & \mathbf{-0.761} & \mathbf{1.864} & 0 \\ \mathbf{-0.695} & \mathbf{-1.847} & 0 & \mathbf{-0.240} & 0 & \mathbf{4.686} \end{pmatrix}. \tag{24}$$

The maximum error in the estimated stiffness components, which are typeset in bold in matrix 24 to facilitate the comparison, is 0.13 $\mathrm{km}^2/\mathrm{s}^2$ for c'_{45} and c'_{46}. This result is certainly satisfactory. Note that rotating tensor $\mathbf{c}'^{(\mathrm{inv})}$ with matrix $(\mathbf{U}^T)^T = \mathbf{U}$ back to the original coordinate frame would lead to greater errors. They are caused by the optimal closeness of $\mathbf{c}'^{(\mathrm{inv})}$ to isotropy and the absence of this property in tensor $\mathbf{c}'$ (compare the upper-left 3×3 blocks in matrices 23 and 24).

In our second example, we use the same fan of directions but remove the slow S-wave phase velocities from the data. Although Figure 9a indicates a different sequence of c'_{IJ}s than Figure 9b, our inversion strategy remains the same. This time, the RMS errors reach a plateau when the data are fitted with a model that contains eight stiffness coefficients. A comparison of the model stiffnesses (equation 23 with the estimated ones (in $\mathrm{km}^2/\mathrm{s}^2$),

$$\mathbf{c}'^{(\mathrm{inv})} = \begin{pmatrix} \mathbf{10.930} & 4.634 & 4.634 & 0 & \mathbf{0.310} & \mathbf{-0.780} \\ 4.634 & 10.930 & 4.634 & 0 & 0 & \mathbf{-1.866} \\ 4.634 & 4.634 & 10.930 & 0 & 0 & 0 \\ 0 & 0 & 0 & 3.148 & 0 & \mathbf{-0.327} \\ \mathbf{0.310} & 0 & 0 & 0 & \mathbf{1.669} & \mathbf{0.415} \\ \mathbf{-0.780} & \mathbf{-1.866} & 0 & \mathbf{-0.327} & \mathbf{0.415} & \mathbf{4.626} \end{pmatrix}, \tag{25}$$

reveals overall greater errors with the largest being about 0.4 $\mathrm{km}^2/\mathrm{s}^2$ for c'_{56}.

Even though a higher uncertainty can be expected in the second test because we use less data to infer the same model parameters as those in the previous example, the obtained results are remarkable in their ability to establish the presence of seismic anisotropy in our

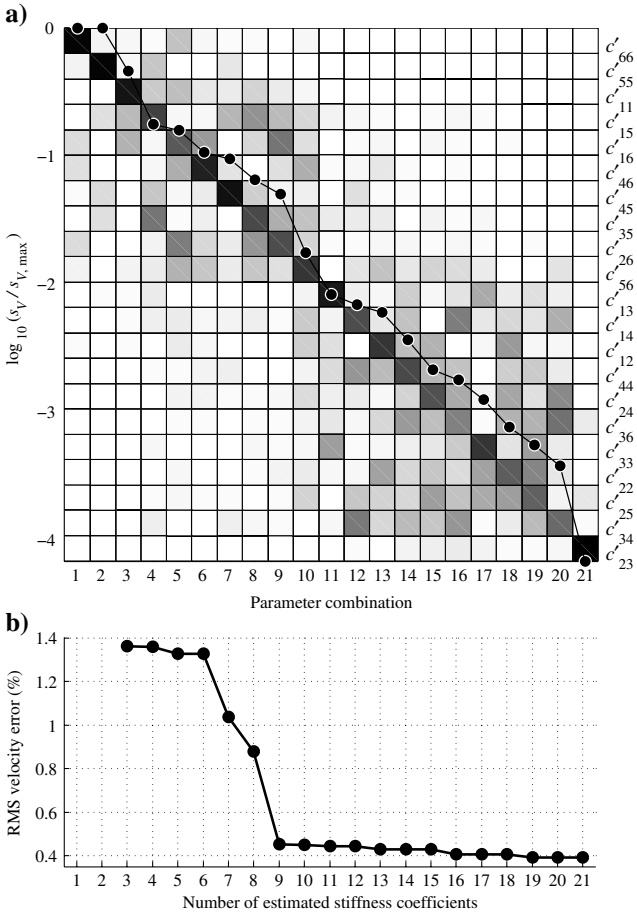

Figure 8. (a) SVD of the phase velocities of the P-, S_1-, and S_2-waves in a fan of wavefront normal directions $\Omega = [40^\circ \le \theta_1 \le 50^\circ, 40^\circ \le \theta_2 \le 50^\circ]$ and (b) behavior of the RMS velocity errors in the course of inversion. Fan Ω contains 25 wavefront normal directions at increments 2.5° in both θ_1 and θ_2.

narrow-angle geometry without relying on the shear-wave splitting. We believe that this happens because of the data sensitivity to the difference in slopes of the wavefront segments corresponding to the P- and S_1-waves. Once a medium homogeneity is assumed, anisotropy provides the only plausible explanation for a misalignment of portions of the wavefronts (or the phase-velocity surfaces) corresponding to different wave modes.

In the next section, we show that the same logic would allow us to establish and estimate seismic anisotropy from our field data despite the velocity heterogeneity of the subsurface.

FIELD-DATA EXAMPLE

Here we apply the developed methodology to build an anisotropic velocity model from perforation-shot data recorded at one stage of hydraulic well treatment in a shale-gas play in the continental United States. The shot-receiver geometry is displayed in Figure 10 in a local coordinate frame whose origin is placed at the shallowest geophone. Figure 10d shows the ray directions plotted on a unit sphere under the assumption of the velocity homogeneity. The ranges of the polar ray angles $31^\circ \le \theta_1 \le 44^\circ$ and the azimuths $-150^\circ \le \theta_2 \le -163^\circ$ (from east to north) clearly indicate a narrow-angle data geometry.

The recorded seismic traces are presented in Figure 11. We rotate the original three-component (3C) data to project particle motions of the direct P-waves (their times are marked with the red ticks) on the first component (Figure 11a, 11c, and 11e). Next, we rotate the remaining two components of data around this component to enhance a wave that arrives next on the second component (Figure 11b, 11d, and 11f). Because, by definition, the second component is orthogonal to the first component, the wave whose traveltimes are shown with the blue ticks in Figure 11 is the direct shear wave. After those two rotations, the third data component contains little coherent energy (not shown), making it impossible for us to determine whether the shear arrival is the fast S_1- or slow S_2-wave. We interpret it as the S_1-wave and acknowledge the implications of our interpretation for the stiffness coefficients that we intend to estimate.

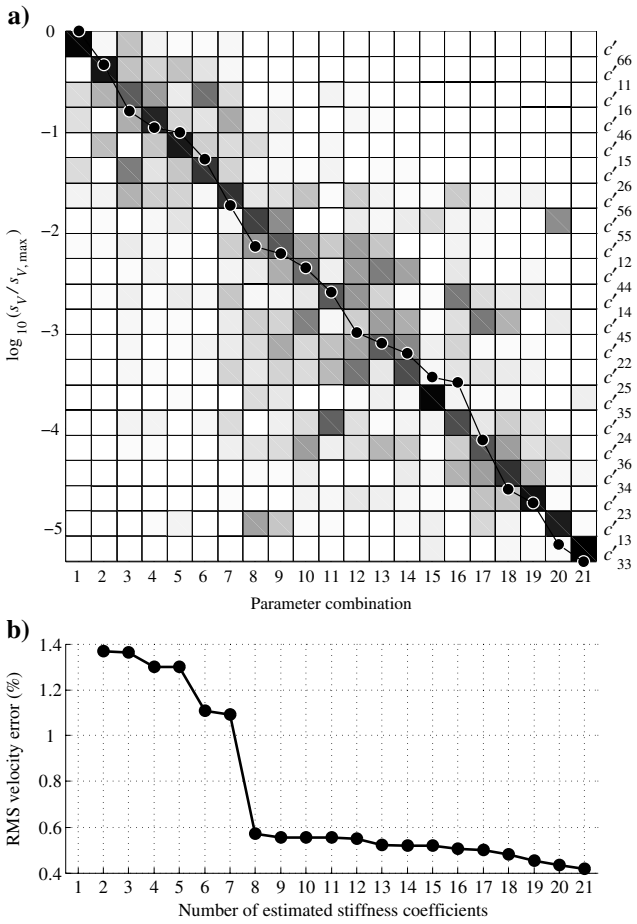

Figure 9. The same as Figure 8 but when phase velocities of the P- and S_1-waves only comprise the data for inversion.

In the following, we will be constructing a velocity model using traveltimes t_Q of the P- and (presumed) S_1-waves. These traveltimes were picked from the data (red and blue ticks in Figure 11) with a precision of one time sample $\Delta t = 0.375$ ms.

Isotropic velocity models

We begin building a seismic velocity model under the simplest assumption that the subsurface is isotropic and homogeneous. Therefore, our model has just two parameters: the P- and S-wave velocities, $V_{\mathrm{P,iso}}$ and $V_{\mathrm{S,iso}}$, respectively. To those we have to add the origin times τ_i $(i = 1, 2, 3)$ of three perforations shots because the shots were not timed. Fitting the traveltime picks in Figure 11 with these five parameters results in the RMS traveltime misfit $\Delta t_{\mathrm{RMS}} = 0.810$ ms. Even though it is significantly greater than the picking precision $\Delta t = 0.375$ ms, the issue of whether or not the obtained homogeneous isotropic model is reasonable can be resolved based on the values of the best-fit isotropic velocities $V_{\mathrm{P,iso}} = 2.870$ km/s and $V_{\mathrm{S,iso}} = 1.993$ km/s. They yield the Poisson's ratio

$$\nu = \frac{V_{\mathrm{P,iso}}^2 - 2V_{\mathrm{S,iso}}^2}{2(V_{\mathrm{P,iso}}^2 - V_{\mathrm{S,iso}}^2)} = 0.034, \tag{26}$$

which is too low for any realistic subsurface rocks. Clearly, this model should be deemed unacceptable on the grounds of rock physics.

To understand what might have caused such a low Poisson's ratio, let us observe that the moveouts of direct arrivals in Figure 11 are close to straight lines (in fact, they are slightly curved, but the curvatures are too small to see them clearly). Therefore, the moveout slopes comprise the key data feature that has to be explained by our homogeneous isotropic model. Because the well containing the geophones is nearly vertical (Figure 10a, 10b, and 10c), the slopes in Figure 11 are approximately equal to the vertical slowness components

$$p_{3,\mathrm{P}} = \frac{\cos\theta_{1,\mathrm{P}}}{V_{\mathrm{P,iso}}} \tag{27}$$

and

$$p_{3,\mathrm{S}} = \frac{\cos\theta_{1,\mathrm{S}}}{V_{\mathrm{S,iso}}}. \tag{28}$$

It is important to note that two polar angles in equations 27 and 28 are equal

$$\theta_{1,\mathrm{P}} = \theta_{1,\mathrm{S}} \tag{29}$$

for each shot-receiver pair because these angles are calculated in a homogeneous isotropic model. Hence, the measured slopes $p_{3,P}$ and $p_{3,S}$ relate to the velocity ratio as

$$\frac{p_{3,S}}{p_{3,P}} = \frac{V_{P,iso}}{V_{S,iso}} \tag{30}$$

and can be used to estimate the effective Poisson's ratio.

Table 2 lists the ratios of the moveout slopes picked from perforation-shot gathers in Figure 11 and the Poisson's ratios calculated using equations 26 and 30. Clearly, the quoted value $\nu = 0.034$ is close to an average Poisson's ratio and, thus, is required to fit the data by a homogeneous isotropic model.

To make further progress and obtain a more satisfactory velocity model, we have the following three options. First, we might keep the assumption of isotropy and build a heterogeneous model. The heterogeneity is supposed to bend rays in such a way as to break down equations 29 and 30 while keeping the correct moveout slopes and yielding physically reasonable Poisson's ratios. Second, we might maintain the homogeneity and evaluate the influence of anisotropy on the obtained traveltimes t_Q. And, third, we might combine the two options above and allow our model to be both

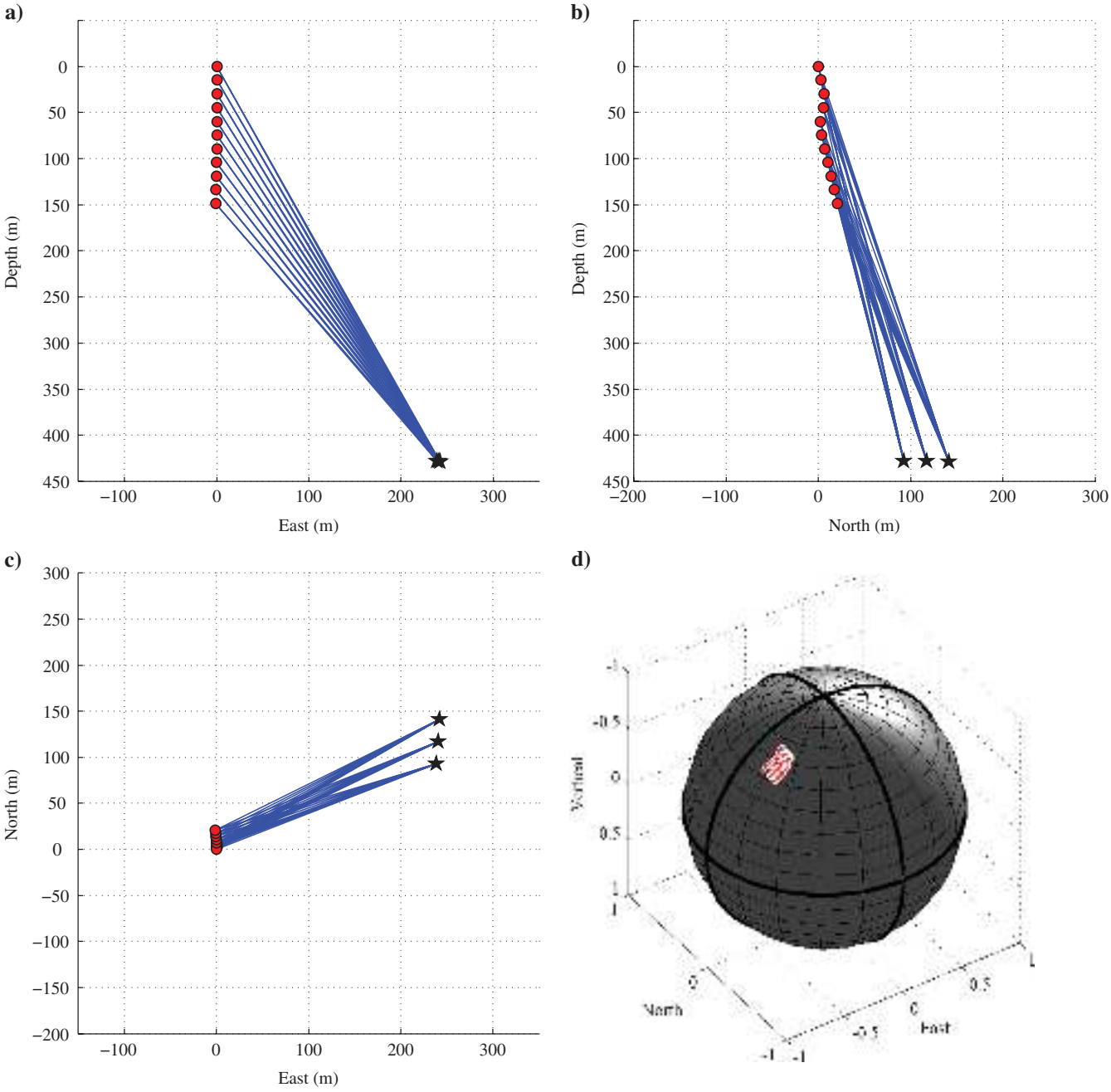

Figure 10. (a, b) Depth and (c) plan views of the locations of three perforation shots (stars) and eleven geophones (circles), and (d) directions of straight rays plotted on a unit sphere.

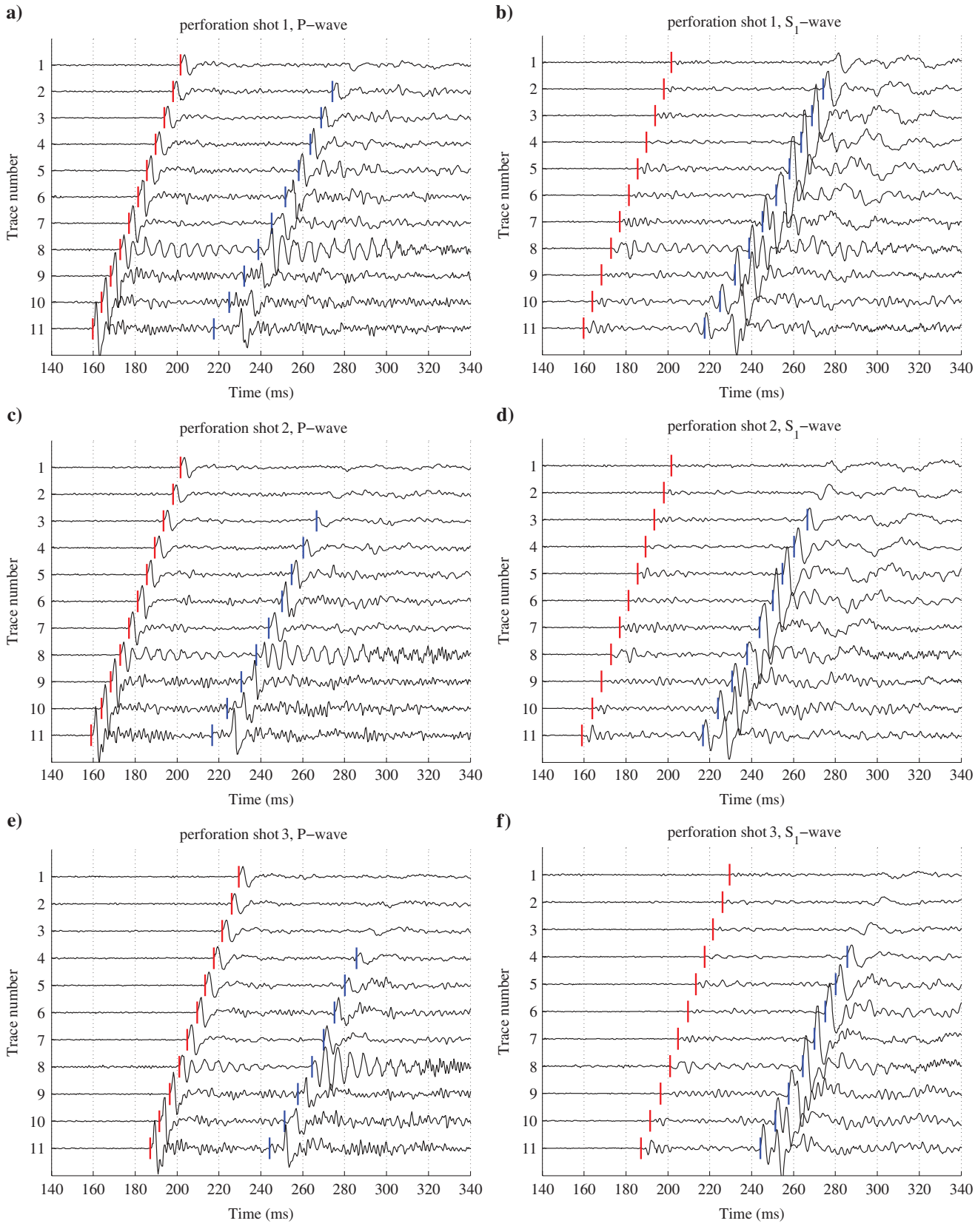

Figure 11. Records of perforation shots number 1 (a, b), 2 (c, d), and 3 (e, f). The 3C traces are rotated to enhance the direct P-waves on one component (a, c, e) and the direct (presumably fast) S-waves – on another (b, d, f). Traveltime picks t_Q of the P- and S_1-waves are shown with red and blue ticks, respectively.

heterogeneous and anisotropic. Let us investigate these options starting with the first.

Conventional velocity models for microseismic data processing consist of isotropic horizontal layers (e.g., Pei et al., 2009, and references therein). Rather than discuss our model of this kind, we analyze those provided to us by microseismic service companies. The first model, constructed by a service company that acquired the data, is shown in Figure 12 (blue) along with the sonic logs (black), which were used as soft constraints to seismic velocities. Let us note that, to honor traveltimes of the perforation shots (Figure 11), the P-wave velocity has been slowed down compared to the sonic by about 700 m/s in the depth range covered by the geophones, that is, exactly in the interval in which the velocities are constrained by the data.

If we take the model velocities (blue in Figure 12) and calculate the Poisson's ratios using equation 26, we obtain the blue staircase line in Figure 13. It is to be compared with the Poisson's ratios (black) derived from the sonic logs in Figure 12. Clearly, the blue staircase Poisson's ratio exhibits the same problem that we experienced with our homogeneous isotropic velocity model: the implausible zero values in the depth range covered by the geophones.

Shell E&P Company has contracted another microseismic service provider to reprocess the data. Its velocity model yields the Poisson's ratios shown in Figure 13 with a dashed green line. We observe not only a "confirmation'' of $\nu = 0$ in a portion of the interval containing the geophones but also a layer at about 300 m depth characterized by the negative Poisson's ratio $\nu = -0.05$. Evidently, the adopted assumption of isotropy fails to produce physically reasonable velocity models.

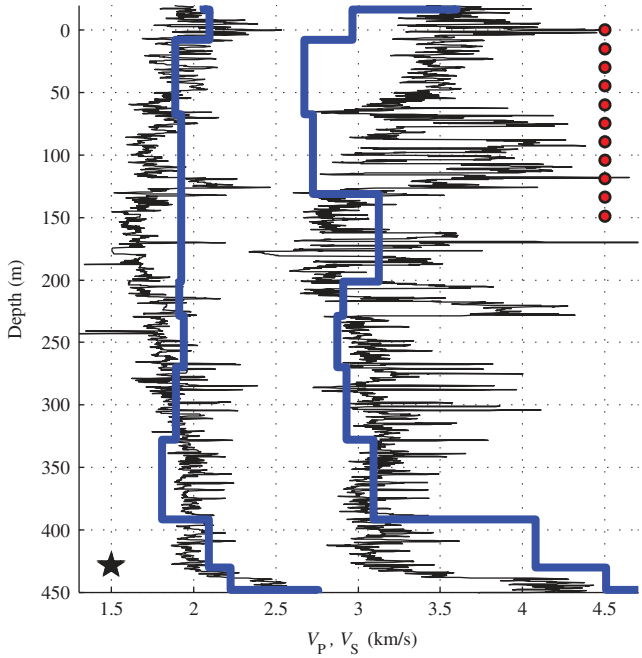

Figure 12. Sonic logs (black) and a horizontally layered isotropic velocity model (blue) built by a microseismic service company. The circles and (overlapping) stars indicate the depths of the geophones and perforation shots, respectively.

Anisotropic models

Let us explore the second option and invert the perforation-shot times t_Q for a suite of homogeneous anisotropic models. In general, we proceed the same way as we did in the section on inversion of the phase velocities but with two obvious differences: we include the origin times τ_i $(i = 1, 2, 3)$ of the perforation shots as additional unknowns and use the Frechét derivatives relevant to the traveltime inversion

$$\mathcal{F}_t \equiv \frac{\partial t_Q}{\partial c'_{IJ}} = -\frac{t_Q}{g_Q}\frac{\partial g_Q}{\partial c'_{IJ}}, \qquad (Q = 1, 2), \qquad (31)$$

where derivatives of the group velocities $\partial g_Q/\partial c'_{IJ}$ are given in Appendix A. The stiffnesses c'_{IJ} relate to those in the global coordinates in Figure 10 via the matrix

Table 2. Ratios of the moveout slopes $p_{3,S}/p_{3,P}$ picked from seismic traces in Figure 11 and the Poisson's ratios calculated with equations 26 and 30.

Perforation-shot number	Ratio of slopes $p_{3,S}/p_{3,P}$	Poisson's ratio
1	1.480	0.080
2	1.446	0.041
3	1.370	−0.070

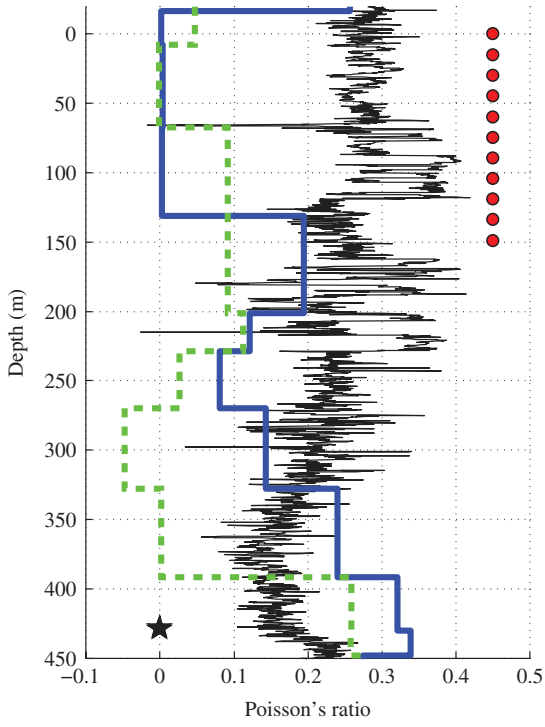

Figure 13. Poisson's ratios calculated using seismic velocities shown in blue in Figure 12 (solid blue) and provided by a different microseismic service company for the same data set (dashed green). Thin black line is the Poisson's ratio derived from the sonic logs in Figure 12.

$$\mathbf{U}^T = \begin{pmatrix} -0.569 & -0.191 & -0.800 \\ 0.590 & 0.583 & -0.558 \\ 0.573 & -0.790 & -0.219 \end{pmatrix}, \qquad (32)$$

which was derived from the polarization (or hodogram) analysis of seismic data in Figure 11 and corresponds to the source-receiver pair exhibiting the greatest linearity of the P-wave particle motion (the linearity is defined by equation C-2 in Grechka and Mateeva, 2007).

Figure 14a displays the results of the SVD of matrix $\mathcal{F}_t$ constructed for the homogeneous isotropic velocity model discussed in the previous section. (Note that full Frechét-derivative matrix for the examined inverse problem contains $\mathcal{F}_t$ augmented by derivatives with respect to the origin times $\partial t_{Q,j}/\partial \tau_i = \delta_{ij}$, where $i,j = 1,2,3$. The latter are excluded from the analysis presented in Figure 14a.) As we gradually increase the number of stiffnesses estimated by the nonlinear inversion, the traveltime misfit reduces to levels below the sampling interval $\Delta t = 0.375$ ms (horizontal dashed line Figure 14b).

While there is some ambiguity about which anisotropic model might be accepted as a solution, we note that such a model cannot contain more than 15 uniquely determined parameters. The number

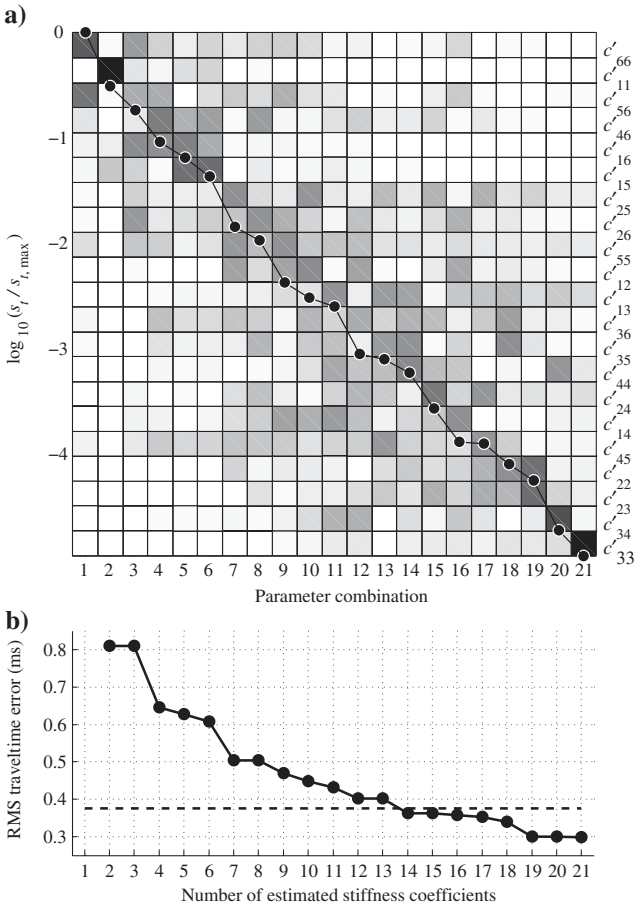

Figure 14. (a) Logarithms of normalized singular values $\mathbf{s}_t$ (black dots) and absolute values of elements of eigenvector matrix $\mathbf{w}_t$ (gray squares) of the Frechét-derivative matrix $\mathcal{F}_t$ (equation 31) for the geometry shown in Figure 10 and (b) RMS errors of perforation-shot times as a function of the number of estimated c'_{IJ}s. The horizontal dashed line in (b) indicates the time sampling interval.

15 follows from a straightforward analysis of the perforation-shot data. Indeed, the traveltimes in each shot gather in Figure 11 are fully represented by six quantities: the origin time τ_i, the difference between arrival times of the shear- and P-waves at any geophone, two moveout slopes, and two moveout curvatures. Six constraints per shot times three shots yield 18 constraints; three of which have to be used to resolve the event-origin times τ_i. With these considerations in mind, we choose the model described by 14 stiffness coefficients. It has the RMS traveltime misfit $\Delta t_{\mathrm{RMS}} = 0.361$ ms, which is just below the time sample, and the stiffness coefficients (in km^2/s^2)

$$\mathbf{c}' = \begin{pmatrix} 8.136 & 1.803 & 3.742 & 0 & -0.179 & 0.079 \\ 1.803 & 9.669 & 2.389 & 0 & 1.762 & -0.025 \\ 3.742 & 2.389 & 9.669 & 0 & -0.057 & 0.263 \\ 0 & 0 & 0 & 4.146 & 0 & -0.129 \\ -0.179 & 1.762 & -0.057 & 0 & 3.623 & 0.067 \\ 0.079 & -0.025 & 0.263 & -0.129 & 0.067 & 3.916 \end{pmatrix}. \qquad (33)$$

There exist several ways of assessing whether the obtained stiffness tensor is plausible. First, we compare its prediction of the vertical velocities with the well logs. Although we realize that high precision of these velocities cannot be expected because they have to be calculated based on extrapolation of the inversion results by more than 30° away from the recorded aperture, we nevertheless apply matrix $\mathbf{U}$ (its transpose is given by equation 32) to rotate tensor 33 to the geographic coordinates. This yields (in km^2/s^2)

$$\mathbf{c} = \begin{pmatrix} 9.350 & 1.923 & 1.960 & 1.003 & -0.017 & -0.401 \\ 1.923 & 10.359 & 3.171 & 0.047 & 0.049 & 0.381 \\ 1.960 & 3.171 & 9.526 & 0.173 & -0.917 & -0.499 \\ 1.003 & 0.047 & 0.173 & 2.937 & -0.226 & 0.119 \\ -0.017 & 0.049 & -0.917 & -0.226 & 3.874 & -0.828 \\ -0.401 & 0.381 & -0.499 & 0.119 & -0.828 & 3.993 \end{pmatrix} \qquad (34)$$

and results in the P- and fast S-wave vertical velocities $V_{\mathrm{P}} = 3.169$ km/s and $V_{\mathrm{S}_1} = 2.074$ km/s, respectively. These velocities are well within the intervals of variation of sonic logs in Figure 12. As another qualitative check, one might calculate the Poisson's ratio corresponding to these V_{P} and V_{S_1}. Even though using equation 26 for this purpose is not entirely appropriate because the medium is anisotropic, such a calculation gives $\nu = 0.18$, which is again a plausible value according to the log in Figure 13. In addition, the relative deviation $\|\mathbf{c} - \mathbf{c}^{\mathrm{iso}}\|/\|\mathbf{c}\|$ of tensor $\mathbf{c}$ from its best-fit isotropic approximation $\mathbf{c}^{\mathrm{iso}}$ (computed in the euclidian norm B1) of about 20% suggests an overall moderate degree of seismic anisotropy, which is certainly expected in our shale-gas field.

The model given by equation 34 can be also verified by using it to find the locations of the perforation shots and compare them with those obtained from an available well-deviation survey (the crosses in Figure 15). To locate the shots, we define a rectangular grid in the vertical planes specified by the average shot azimuths (see Figure 10c) and treat each grid point $\boldsymbol{\zeta}$ as a potential shot position. We then calculate traveltimes $t_{Q,i}(\boldsymbol{\zeta}) + \tau_i$ $(i = 1,2,3)$ in our homogeneous triclinic model and post the RMS misfits $\Delta t_{\mathrm{RMS}}(\boldsymbol{\zeta})$ between these traveltimes and the times picked at Figure 11 at each $\boldsymbol{\zeta}$. Figure 15 presents the result of our computation performed

on a square grid with the grid size $\Delta\zeta = 2$ m. We accurately fit both the traveltime picks (the maximum of Δt_{RMS} is 0.38 ms) and the spatial positions of the perforation shots (the maximum deviation of min Δt_{RMS} from the corresponding shot location is 2 m), which, in retrospect, justifies our interpretation of the recorded shear arrivals as the S_1-waves. Clearly, comparison of the shot locations disregards possible errors in the well-deviation survey, which might not only influence the positions of crosses in Figure 15 but also bias the estimates of stiffness coefficients in matrices 33 and 34 (Bulant et al., 2007).

In summary, the obtained homogeneous anisotropic velocity model satisfactorily describes the available perforation-shot times, places the shots at their correct locations, and agrees with the well logs. Our model contains 14 stiffness coefficients, which nearly exhaust the maximum number of quantities that can be unambiguously estimated. Thus, we conclude that introducing heterogeneity is unnecessary to fit our field data.

DISCUSSION

The presented study had two main objectives. The first was to ensure the uniqueness of inversion of seismic anisotropy. We realized that the estimation of the elastic stiffness coefficients from seismic velocities measured in narrow-angle geometries (which are typical for downhole microseismic surveys) has to be performed in a specially rotated coordinate frame to avoid ambiguity. We suggested to select this frame by aligning its coordinate axes with the polarization vectors of three plane waves propagating along any direction within a given data aperture. This choice resulted in a significant simplification of equations describing the phase and group velocities in anisotropic media and made it possible to gain analytic insights into which stiffness coefficients c'_{IJ} in the rotated frame are constrained by the data (see equations 13–15).

It was natural then that we targeted these c'_{IJ}s in the inversion. Our numerical tests corroborated the analytic results and demonstrated that, indeed, the accurate estimation of certain c'_{IJ}s from noise-contaminated seismic velocities is possible. Along the way, we encountered an interesting problem of infilling the c'_{IJ}s unconstrained by our data. It is quite obvious that some additional information had to be brought in to assign numerical values to these stiffness coefficients. We have chosen to draw this information from the requirement that the inverted stiffness tensor $\mathbf{c}'$ is as close to isotropy as possible. Clearly, this is not the only option. Other options include approximating the symmetry of $\mathbf{c}'$ with either transverse isotropy (TI) of orthotropy. Because TI and orthorhombic media are characterized by more independent stiffness coefficients than isotropy, they are expected to represent $\mathbf{c}'$ better. We have not followed this path, however, primarily because it implies the availability of a priori knowledge of the medium symmetry. Although the symmetry was certainly known in our synthetic examples, this was not the case with the field data. For this reason, we decided to leave the problem of finding the best TI or orthorhombic approximation to an incompletely known stiffness tensor to a future study.

The second goal of our paper was to test the developed anisotropic parameter-estimation methodology on field data. Although, ideally, one would like to build a single, possible time-dependent, model that explains perforation-shot and microseismic data recorded in an entire survey (a more modest attempt is presented in a companion paper by Grechka et al., 2011), here we followed conventional practice, according to which velocity models for each

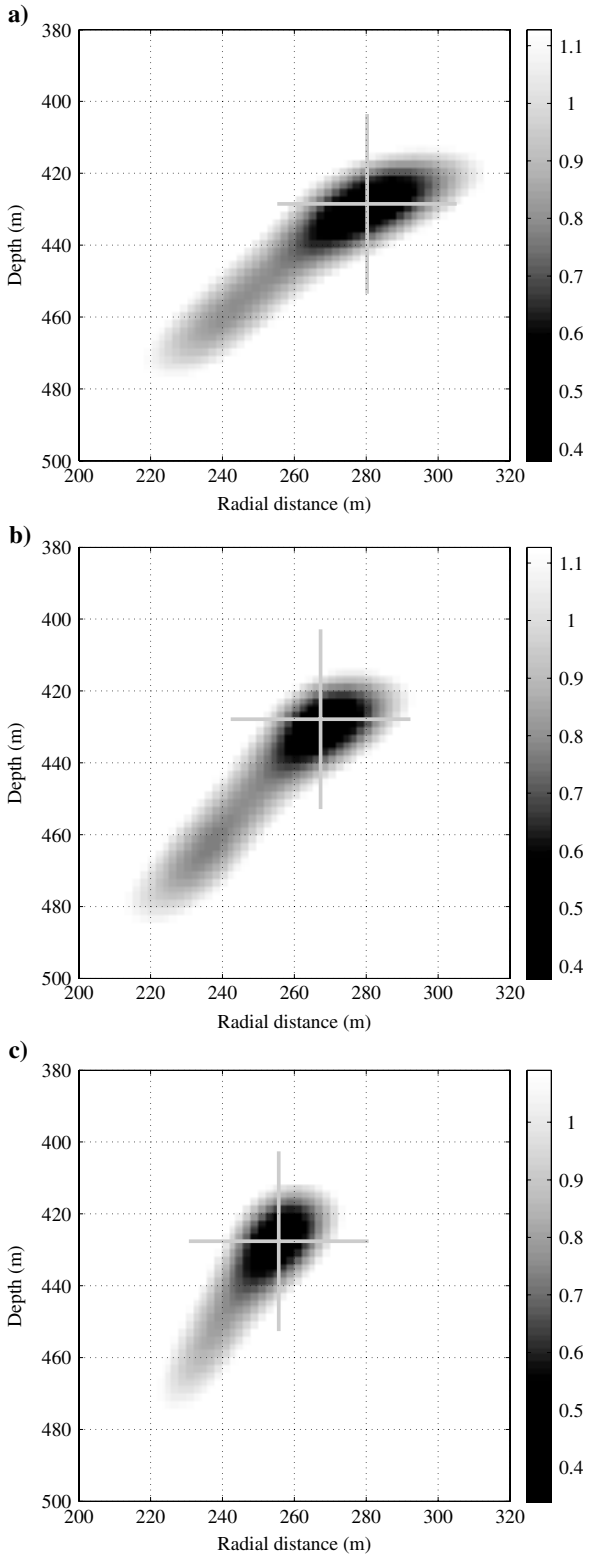

Figure 15. Sections of Δt_{RMS} (in ms) for three perforation shots (arranged from north to south) in the vertical planes specified by the perforation-shot azimuths (Figure 10c). Calculations are performed in the triclinic model given by equation 34. The size of color bars in all panels is equal to 0.75 ms or to two time samples. The crosses mark locations of the perforation shots based on the well-deviation survey.

stage of hydraulic well stimulation are constructed using perforation shots acquired at that stage. We managed to derive a homogeneous anisotropic velocity model that fits the times of the P- and fast S-waves picked from perforation-shot data in Figure 11 with the RMS error smaller than one time sample in the data. Importantly, our model predictions of the vertical velocities are consistent with the available well logs. In contrast, either homogeneous or layered isotropic velocity models examined in the paper exhibit unrealistically low or even negative Poisson's ratios.

We conclude our paper by observing that anisotropic velocity-model building for microseismic data processing is in its infancy. While hundreds of authors discuss anisotropy in the context of seismic reflection data, we are aware of only a few publications (Teanby et al., 2004; Maxwell et al., 2006; Michaud et al., 2009) that describe estimation of anisotropy for microseismic monitoring. This makes us believe that a significant body of work needs to be done to develop practical approaches for measuring seismic anisotropy in microseismic geometries and using it to improve our knowledge of the properties of hydraulically treated formations.

CONCLUSIONS

Our paper contains both theoretical and practical contributions. On the theoretical side, we demonstrated how to estimate elements of the elastic stiffness tensor from seismic velocities or traveltimes measured in narrow-angle geometries. We showed that such an inversion has to be performed in rotated coordinates to ensure its uniqueness. In addition to identifying the stiffness components that can be unambiguously inverted, we derived the equation for the group velocities in generally anisotropic (triclinic) media that happened to be computationally superior to many other known equations.

Our practical contribution includes building a triclinic velocity model from field perforation-shot data. The constructed model fits the traveltime picks of the P- and fast S-waves within one time sample and resolves the issue with unrealistically low Poisson's ratios inherent for isotropic velocity models derived from the same traveltimes.

ACKNOWLEDGMENTS

We thank Shell E&P Company and EnCana for the permission to publish our paper, as well as GEOPHYSICS guest editor J.-M. Kendall and two anonymous reviewers for their thorough reviews and numerous useful suggestions.

APPENDIX A

FRECHÉT DERIVATIVES OF SEISMIC VELOCITIES

The goal of this Appendix is to derive the Frechét derivatives $\mathcal{F}_V \equiv \partial V_Q/\partial c_{IJ}$ and $\mathcal{F}_g \equiv \partial g_Q/\partial c_{IJ}$ $(Q = 1,2,3;\ I,J = 1,\ldots,6)$ of the phase and group velocities V_Q and g_Q, with respect to the stiffness components c_{IJ}.

Derivatives of phase velocities

Because the phase velocities are calculated from the Christoffel equation 1 in direction of the unit wavefront normal $\mathbf{n}$, it is natural to evaluate the derivatives $\partial V_Q/\partial c_{IJ}$ at a fixed $\mathbf{n}$. Following the approach described in Zhou and Greenhalgh (2005), we rewrite equation 1 in the form

$$V_Q^2 U_{iQ} = c_{ijkl} n_j n_k U_{lQ}, \qquad (i,Q = 1,2,3) \tag{A-1}$$

and use the fact that the polarization vectors $\mathbf{U}_Q$ are mutually orthogonal, because they are the eigenvectors of equation A-1. Hence:

$$\mathbf{U}_Q \cdot \mathbf{U}_R = \delta_{QR}, \qquad (Q,R = 1,2,3), \tag{A-2}$$

where δ_{QR} is the 3×3 identity matrix. Taking a dot product of equation A-1 and vector $\mathbf{U}_R$ yields

$$V_Q^2 \delta_{QR} = c_{ijkl} U_{iR} n_j n_k U_{lQ}, \qquad (Q,R = 1,2,3). \tag{A-3}$$

Next, we set $R = Q$ in equation A-3 and differentiate it with respect to components of the stiffness tensor. The result reads

$$2V_Q \frac{\partial V_Q}{\partial c_{i'j'k'l'}} = U_{i'Q} n_{j'} n_{k'} U_{l'Q} + 2c_{ijk\ell}\left(\frac{\partial U_{iQ}}{\partial c_{i'j'k'l'}}\right) n_j n_k U_{lQ}, \qquad (i',j',k',l',Q = 1,2,3). \tag{A-4}$$

To prove that the second term in equation A-4 vanishes, we note that any derivative of $\mathbf{U}_Q$ projects onto two orthogonal polarization vectors $\mathbf{U}_{R_1}$, $\mathbf{U}_{R_2}$ $(R_1 \neq R_2 \neq Q)$ because $\mathbf{U}_Q$ is a unit vector and apply equation A-3. Therefore,

$$\frac{\partial V_Q}{\partial c_{ijkl}} = \frac{1}{2V_Q} U_{iQ} n_j n_k U_{lQ}, \qquad (i,j,k,l,Q = 1,2,3). \tag{A-5}$$

The derivatives $\mathcal{F}_V = \partial V_Q/\partial c_{IJ}$ are obtained from those in equation A-5 using the standard substitutions $11 \to 1$, $22 \to 2$, $33 \to 3$, $23 \to 4$, $13 \to 5$, and $12 \to 6$ for the pairs of indexes of c_{ijkl} and the symmetry $c_{IJ} = c_{JI}$ of a Voigt stiffness matrix. To account for this symmetry, the derivatives $\partial V_Q/\partial c_{IJ}$ need to be multiplied by $(2 - \delta_{IJ})$. We note that equation A-5 is inapplicable to the S-waves at their point singularities $\mathbf{n}^S$, because the polarization vectors $\mathbf{U}_Q$ $(Q = 2,3)$ are nonuniquely defined at $\mathbf{n} = \mathbf{n}^S$ (e.g., Fedorov, 1968).

Derivatives of group velocities

To derive the Frechét derivatives $\mathcal{F}_g \equiv \partial g_Q/\partial c_{IJ}$, it is convenient to start with the equality (e.g., Auld, 1973)

$$\mathbf{g} \cdot \mathbf{p} = 1, \tag{A-6}$$

where $\mathbf{g}$ is the group-velocity vector, $\mathbf{p}$ is the corresponding slowness vector, and the wave-type identifier $Q = 1,2,3$ is omitted for brevity. Defining the unit ray vector $\mathbf{r}$ through equation

$$\mathbf{g} = |\mathbf{g}|\mathbf{r} \equiv g\mathbf{r}, \tag{A-7}$$

we rewrite equation A-6 as

$$g(\mathbf{r} \cdot \mathbf{p}) = 1. \tag{A-8}$$

The reason for introducing vector $\mathbf{r}$ is that the most useful derivatives $\partial g/\partial c_{IJ}$ are obtained at a fixed ray direction, that is, $\partial g/\partial c_{IJ}|_{\mathbf{r}=\text{const}}$. Indeed, such derivatives can be directly applied to evaluate the Frechét derivatives of traveltimes (see equation 31) because the latter correspond to stationary ray trajectories in accordance with Fermat's principle. With this in mind, we differentiate equation A-8 with respect to c_{IJ}

$$\frac{\partial g}{\partial c_{IJ}}(\mathbf{r}\cdot\mathbf{p})+g\left(\frac{\partial \mathbf{r}}{\partial c_{IJ}}\cdot\mathbf{p}\right)+g\left(\mathbf{r}\cdot\frac{\partial \mathbf{p}}{\partial c_{IJ}}\right)=0, \quad (I,J=1,\ldots,6). \tag{A-9}$$

Taking into account that the second term in equation A-9 vanishes because $\mathbf{r}=\text{const}$ and using equation A-8, we obtain

$$\frac{\partial g}{\partial c_{IJ}}=-g^2\left(\mathbf{r}\cdot\frac{\partial \mathbf{p}}{\partial c_{IJ}}\right), \qquad (I,J=1,\ldots,6). \tag{A-10}$$

To proceed further, we need to derive the Frechét derivatives of the slownesses $\partial\mathbf{p}/\partial c_{IJ}$. Those are found by differentiating the condition

$$F(\mathbf{p},\mathbf{c})\equiv\det[c_{ijkl}p_jp_k-\delta_{il}]=0 \tag{A-11}$$

for the existence of nonzero eigenvectors of the Christoffel equation. Applying the chain rule to equation A-11 yields

$$\frac{\partial F}{\partial c_{IJ}}=-\frac{\partial F}{\partial p_i}\frac{\partial p_i}{\partial c_{IJ}}=-\left(\nabla_{\mathbf{p}}F\cdot\frac{\partial \mathbf{p}}{\partial c_{IJ}}\right), \qquad (I,J=1,\ldots,6), \tag{A-12}$$

where $\nabla_{\mathbf{p}}F$ is the gradient of F in the slowness space. Being the gradient, $\nabla_{\mathbf{p}}F$ is orthogonal to the slowness surface given by equation A-11 and, hence, parallel to the group-velocity vector and ray $\mathbf{r}$ (e.g., Auld, 1973; Helbig, 1994). The latter means that

$$\frac{\partial F}{\partial c_{IJ}}=-|\nabla_{\mathbf{p}}F|\left(\mathbf{r}\cdot\frac{\partial \mathbf{p}}{\partial c_{IJ}}\right), \qquad (I,J=1,\ldots,6) \tag{A-13}$$

and, as follows from equation A-10,

$$\mathcal{F}_g=\frac{\partial g}{\partial c_{IJ}}=\frac{g^2}{|\nabla_{\mathbf{p}}F|}\frac{\partial F}{\partial c_{IJ}}, \qquad (I,J=1,\ldots,6), \tag{A-14}$$

where derivatives $\partial F/\partial c_{IJ}$ and gradient $\nabla_{\mathbf{p}}F$ are calculated by differentiating determinant A-11.

Like equation A-5, equation A-14 cannot be used at point singularities, where gradient $\nabla_{\mathbf{p}}F$ is undefined. Also equation A-14 is expected to break down for rays $\mathbf{r}^C$ corresponding to the tips of cusps that are always present at the shear wave group-velocity surfaces for symmetries lower than transverse isotropy. Indeed, a general stiffness perturbation is expected to move a cusp in such a way that $\mathbf{r}^C$ would be placed either in a shadow zone or into a volume in which $g(\mathbf{r}^C)$ is multivalued.

APPENDIX B

ISOTROPIC APPROXIMATION OF INCOMPLETE STIFFNESS TENSOR

Here we discuss how to find the best-fit isotropic stiffness tensor $\mathbf{c}^{\text{iso}}$ to a given tensor $\mathbf{c}$ when some elements of $\mathbf{c}$ are unknown. Our analysis is based on the well-known Fedorov's (1968) solution to the same problem obtained under the condition that all components of $\mathbf{c}$ are available. We revisit the result of Fedorov first and then describe its appropriate modification.

Fedorov (1968) examines the problem of minimizing the function

$$\mathcal{L}\equiv\min_{(\lambda,\mu)}\sum_{i,j,k,l=1}^{3}(c_{ijkl}-c^{\text{iso}}_{ijkl})^2 \tag{B-1}$$

in terms of the Lamé coefficients λ and μ that define $\mathbf{c}^{\text{iso}}$ according to equation

$$c^{\text{iso}}_{ijkl}=\lambda\delta_{ij}\delta_{kl}+\mu(\delta_{ik}\delta_{jl}+\delta_{il}\delta_{jk}), \qquad (i,j,k,l=1,2,3), \tag{B-2}$$

where δ_{ij} is the Kronecker delta. Substituting equation B-2 into equation B-1 and switching to Voigt notation yields

$$\mathcal{L}=\sum_{I=1}^{3}[c_{II}-(\lambda+2\mu)]^2+2\sum_{\substack{J,K=1\\J\neq K}}^{3}(c_{JK}-\lambda)^2+4\sum_{M=4}^{6}(c_{MM}-\mu)^2. \tag{B-3}$$

The Lamé coefficients are found using the standard optimization requirement

$$\frac{\partial\mathcal{L}}{\partial\lambda}=\frac{\partial\mathcal{L}}{\partial\mu}=0, \tag{B-4}$$

which leads to two linear equations for λ and μ. If values of all relevant stiffness coefficients are known, equations B-4 yield the system

$$\begin{aligned}9\lambda+6\mu&=\sum_{I=1}^{3}c_{II}+2\sum_{\substack{J,K=1\\J\neq K}}^{3}c_{JK},\\ 3\lambda+12\mu&=\sum_{I=1}^{3}c_{II}+2\sum_{M=4}^{6}c_{MM},\end{aligned} \tag{B-5}$$

which was analyzed and solved by Fedorov (1968).

When some pertinent c_{IJ}s are unavailable, the corresponding terms have to be removed from the least squares formulation B-3 and derivatives in equations B-4 should be computed for the new misfit function. If, for example, only c_{11}, c_{55}, and c_{66} can be measured, as Figures 3 and 5 might suggest, then the equations to be solved are

$$\lambda+2\mu=c_{11}, \quad \lambda+6\mu=c_{11}+2(c_{55}+c_{66}). \tag{B-6}$$

The solution of system B-6, $\lambda = c_{11} - (c_{55} + c_{66})$ and $\mu = (c_{55} + c_{66})/2$, is obviously different from that of system B-5.

REFERENCES

Auld, B. A., 1973, Acoustic fields and waves in solids, volumes I and II: John Wiley (second edition, 1990, Krieger Publishing).

Bulant, P., L. Eisner, I. Pšenčík, and J. Le Calvez, 2007, Importance of borehole deviation surveys for monitoring of hydraulic fracturing treatments: Geophysical Prospecting, **55**, 891–899, doi: 10.1111/gpr.2007.55.issue-6.

Červený, V., 2001, Seismic ray theory: Cambridge University Press.

Cowin, S. C., 1989, Properties of the anisotropic elastic tensor: Quarterly Journal of Mechanics and Applied Mathematics, **42**, 249–266, doi: 10.1093/qjmam/42.2.249.

Fedorov, F. I., 1968, Theory of elastic waves in crystals: Plenum Press.

Grechka, V., and A. Mateeva, 2007, Inversion of P-wave VSP data for local anisotropy: Theory and a case study: Geophysics, **72**, no. 4, D69–D79, doi: 10.1190/1.2742970.

Grechka, V., P. Singh, and I. Das, 2011, Estimation of effective anisotropy simultaneously with locations of microseismic events: Geophysics, **76**, this volume.

Grechka, V., and I. Tsvankin, 1999, 3D moveout velocity analysis and parameter estimation for orthorhombic media: Geophysics, **64**, 820–837, doi: 10.1190/1.1444593.

Grechka, V., I. Tsvankin, and J. K. Cohen, 1999, Generalized Dix equation and analytic treatment of normal-moveout velocity for anisotropic media: Geophysical Prospecting, **47**, 117–148, doi: 10.1046/j.1365-2478.1999.00120.x.

Helbig, K., 1994, Foundations of anisotropy for exploration seismics: Elsevier.

Helbig, K., and M. Schoenberg, 1987, Anomalous polarization of elastic waves in transversely isotropic media: Journal of the Acoustical Society of America, **81**, no. 5, 1235–1245.

Maxwell, S., 2010, Microseismic: Growth born from success: The Leading Edge, **29**, 338–343, doi: 10.1190/1.3353732.

Maxwell, S., J. Shemeta, and N. House, 2006, Integrated anisotropic velocity modeling using perforation shots, passive seismic and VSP data: CSPG-CSEG-CWLS Convention.

Maxwell, S. C., J. Rutledge, R. Jones, and M. Fehler, 2010, Petroleum reservoir characterization using downhole microseismic monitoring: Geophysics, **75**, no. 5, 75A129–75A137, doi: 10.1190/1.3477966.

Michaud, G. C., W. S. Leaney, L. Bennett, M. McClay, K. Ainsworth, M. Kaiser, and B. McPherson, 2009, Dual treatment monitoring with a horizontal receiver array: EAGE Workshop on Passive Seismic, Limassol, A13.

Pei, D., J. A. Quirein, B. E. Cornish, D. Quinn, and N. R. Warpinski, 2009, Velocity calibration for microseismic monitoring: A very fast simulated annealing (VFSA) approach for joint-objective optimization: Geophysics, **74**, no. 6, WCB47–WCB55, doi: 10.1190/1.3238365.

Press, W. A., S. A. Teukolsky, W. T. Vetterlink, and B. P. Flannery, 2003, Numerical recipes in Fortran 77: The art of scientific computing: Cambridge University Press.

Teanby, N., J.-M. Kendall, R. H. Jones, and O. Barkved, 2004, Stress-induced temporal variations in seismic anisotropy observed in microseismic data: Geophysical Journal International, **156**, 459–466, doi: 10.1111/gji.2004.156.issue-3.

Thomsen, L., 1986, Weak elastic anisotropy: Geophysics, **51**, 1954–1966, doi: 10.1190/1.1442051.

Tsvankin, I., 1997, Anisotropic parameters and P-wave velocity for orthorhombic media: Geophysics, **62**, 1292–1309, doi: 10.1190/1.1444231.

Tsvankin, I., 2001, Seismic signatures and analysis of reflection data in anisotropic media: Pergamon (second edition, 2005).

Warpinski, N. R., R. B. Sullivan, J. E. Uhl, C. K. Waltman, and S. R. Machovoe, 2005, Improved microseismic fracture mapping using perforation timing measurements for velocity calibration: Society of Petroleum Engineers Journal, Paper 84488.

Xiao, X., and W. S. Leaney, 2010, Local vertical seismic profiling (VSP) elastic reverse-time migration and migration resolution: Salt-flank imaging with transmitted P- to S-waves: Geophysics, **75**, no. 2, S35–S49, doi: 10.1190/1.3309460.

Zheng, X., and I. Pšenčík, 2002, Local determination of weak anisotropy parameters from qP-wave slowness and particle motion measurements: Pure and Applied Geophysics, **159**, 1881–1905, doi: 10.1007/s00024-002-8713-z.

Zhou, B., and S. A. Greenhalgh, 2005, Analytic expressions for the velocity sensitivity to the elastic moduli for the most general anisotropic media: Geophysical Prospecting, **53**, 619–641, doi: 10.1111/gpr.2005.53.issue-4.